Solidification depth and crystallization age of the Shiaidani Granodiorite: constraints to the average denudation rate of the Hida Range, central Japan

Tetsuo KAWAKAMI[1, *], Shigeru SUEOKA[2], Tatsunori YOKOYAMA[2], Saya KAGAMI[2], Georgina E. King[3], Frédéric Herman[3], Sumiko Tsukamoto[4] and Takahiro TAGAMI[1]

1: Department of Geology and Mineralogy, Graduate School of Science, Kyoto University, Kitashirakawa-Oiwake-cho, Sakyo-ku, Kyoto 606-8502, Japan

2: Tono Geoscience Center, Japan Atomic Energy Agency, 959-31, Jorinji, Izumi-cho, Toki, Gifu, 509-5102, Japan.

3: Institute of Earth Surface Dynamics, University of Lausanne, Lausanne, Switzerland

4: Leibniz Institute for Applied Geophysics, 30655 Hannover, Germany

* Corresponding author, t-kawakami@kueps.kyoto-u.ac.jp, ORCID ID: https://orcid.org/0000-0002-5921-5562

Abstract

Solidification pressure and crystallization age of the ca. 5 Ma Shiaidani Granodiorite (Hida Mountain Range, central Japan) are determined based on Al-in-hornblende geobarometry and U-Pb zircon dating. Al-poor patchy replacements developed in amphiboles are common in this granite and petrographic study revealed that the replacements include chloritized biotite and albitic plagioclase. These are probably the hydrothermally recrystallized domains, and should not be used for solidification pressure estimates. Magmatic rim of amphibole is characterized by Si < 7.3 a.p.f.u. (Al_{IV} > 0.7 a.p.f.u.), and utilized in solidification pressure estimate that yielded 0.17-0.29 GPa. The solidification age of the granite is estimated as ca. 5.6-5.2 Ma using U-Pb zircon dating. From these data, the lower limit of an average denudation rate after ca. 5.6-5.2 Ma for the area where Shiaidani Granodiorite is exposed is estimated as 0.93-2.5 mm/yr.

Keywords: granite, exhumation, hornblende, patchy zoning

1 Introduction

Emplacement depth of granitoids in the upper continental crust in combination with their solidification ages are useful in reconstructing the complex exhumation and tectonic processes of the region where the granitoids are currently exposed. The Kurobe area, Hida Mountain Range, central Japan is characterized by the exposure of the youngest granites in the world (Ito et al., 2013, 2017), and exhumation history of the young granites have been of great interest (Yamada, 1997; Yamada & Harayama, 1999; Spencer et al., 2019). However, results of low-temperature geochronological methods are often thermally affected by the late-stage granite intrusions (Yamada & Harayama, 1999) and a method to reliably constrain the depth and age information was needed.

The Al-in-hornblende barometer (Anderson & Smith, 1995; Hammarstrom & Zen,1986; Mutch et al., 2016; Schmidt, 1992) has long been used to constrain the solidification pressure of granitoid plutons. In applying the Al-in-hornblende barometer, choosing a right composition of hornblende is very important, because the barometer uses the Al content of amphibole that crystallized at the granite solidus. Mutch et al. (2016) recommended to use amphibole analyses taken from the rims of grains, in contact with plagioclase and in apparent textural equilibrium with the rest of the mineral assemblage at temperatures close to the haplogranite solidus, as determined from amphibole–plagioclase thermometry. However, using the rim composition of amphibole is not a successful criterion in the case of hornblende with patchy Al zoning (e.g., Yamaguchi et al., 2003; Hartung et al., 2017), which is probably a result of post-magmatic hydrothermal alteration. As a criterion of amphibole crystallized under magmatic or subsolidus conditions, Chivas (1981) proposed that amphiboles with Si > 7.3 a.p.f.u. for O = 23 (Al_{IV} < 0.7 a.p.f.u.) are not truly magmatic and crystallized under subsolidus conditions in the presence of a fluid phase. On the other hand, in the study of the

Takidani Pluton (Hida Range), Hartung et al. (2017) considered low-Al and high-Al amphiboles observed as patchy zones could have formed under near-isobaric conditions and difference in Al may be related to the temperature and chemical variability of the melt from which they crystallized (Hartung et al., 2017). Therefore, careful microstructural observation on the coexisting minerals of each amphibole domain is required to understand the development of patchy zones in amphibole, and to finally constrain the solidification pressure of the pluton.

This study examines mode of occurrence and chemical composition of amphibole in the Shiaidani Granodiorite in detail to constrain the formation timing of the patchy domains. We petrographically constrain suitable amphibole domains/compositions that coexisted with the necessary phases to apply the Al-in-hornblende barometry (e.g., Mutch et al., 2016) and estimate the solidification pressure of the Shiaidani Granodiorite. In combination with the U-Pb zircon dating of the granodiorite, average denudation rate after ca. 5.6-5.2 Ma is finally constrained for the area where Shiaidani Granodiorite is exposed. In this study, we follow the definition of “exhumation” and “denudation” by Ring et al. (1999), Reiners and Brandon (2006) and Sueoka and Tagami (2019). “Exhumation” is the vertical distance traveled by rocks relative to Earth’s surface and “denudation” takes into account the lateral movement of the exhumed rocks.

2 Geological setting

The Shiaidani Granodiorite crops out in the Kurobe area, Hida Mountain Range, central Japan (Figure 1). It is exposed as elongate-shaped pluton with a NS length of ~12 km and maximum EW width of ~3 km (Harayama, 2015). The world's youngest granite, the Kurobegawa Granite (ca. 0.8 Ma), is exposed along the Kurobegawa River (Ito et al., 2013; 2017; Spencer et al., 2019). It is accompanied by young volcanics such as 1.7-1.6 Ma Jiigatake Volcanics (mainly rhyolitic welded tuff and andesite and rhyolite lavas) and 1.6 Ma Shirakawa-tengu Volcanics (mainly rhyolitic welded tuff) to the east (Figure 1; Harayama et al., 2015). The Kurobegawa Granite intrudes the Jiigatake Volcanics (Harayama et al., 2010). The Shiaidani Granodiorite is exposed roughly to the west of Kurobegawa River. It was previously considered as a part of the Kurobe-bessan Granite (Harayama et al., 2010), which was divided into the Shiaidani Granodiorite (ca. 5.5-5.4 Ma) and the Kuranosuke Granite (ca. 9.5-9.1 Ma) based on the difference in U-Pb zircon ages (Harayama, 2015; Ito et al., 2013). The Kuranosuke Granite is distributed to the west of the Shiaidani Granodiorite (Figure 1). The Shiaidani Granodiorite is also dated to be ca. 7.1-5.1 Ma and ca. 5.1-4.3 Ma by K-Ar dating of hornblende and biotite, respectively (Ogata et al., 1983; Yamada & Harayama, 1999; Harayama, 2015; Harayama et al., 2010). The zircon fission track age is dated at ca. 1.5 Ma (Harayama et al., 2010). The Kuranosuke Granite, on the other hand, is dated at ca. 5.1 Ma by K-Ar dating of biotite (Harayama et al., 2010). Based on the existence of a decussate structure of biotite, Harayama et al. (2010) considered that recrystallization due to thermal metamorphism was evident in the Kurobe-bessan Granite.

3 Analytical methods

Quantitative analyses of rock-forming minerals and X-ray elemental mapping of thin section samples were performed by a JEOL JXA-8105 superprobe at Kyoto University. Analytical conditions for quantitative analyses were 15.0 kV acceleration voltage, 10 nA beam current, and 3 μm beam diameter. The counting time for the peak and backgrounds were 30 s and 15 s for Cl, 60 s and 30 s for F, and 10 s and 5 s for other elements. Natural and synthetic minerals were used as standards and the ZAF correction was applied. Representative mineral analyses are given in Table 1. Recalculation of ferric iron in amphibole and calculation of amphibole formula are based on Holland and Blundy (1994).

Two granite samples were crushed in a rod mill and stainless steel mortar. Zircon grains were separated by panning, magnetic separation and using heavy liquid at Kyoto Fission-Track Co. Ltd. After handpicking under a stereomicroscope, zircon grains were mounted in epoxy resin (Struers SpeciFix-20). Cathodoluminescence (CL) images of zircon grains were obtained by using a field emission electron microprobe JEOL JXA-8530F at Japan Atomic Energy Agency, Tono Geoscience Center (JAEA, TGC). Analysis points were selected to avoid cracks and inclusions using CL images. U-Pb isotopic analysis by laser ablation−inductively coupled plasma−mass spectrometry (LA−ICP−MS) was performed in JAEA, TGC using Thermo Fisher Scientific Neptune-*Plus* coupled with Photon-Machines Analyte G2 Excimer laser on separate zircon grains. For U-Pb isotope analysis to estimate the zircon crystallization ages, the 91500 zircon (Wiedenbeck et al., 1995, 2004) was used as the primary reference and standard material to correct the mass bias effect on $^{206}Pb/^{238}U$ and $^{207}Pb/^{206}Pb$, respectively. Duplicate measurements of the secondary reference materials of OD-3 (33.0 ±0.1 Ma: Iwano et al., 2013) were carried out to assess the age data obtained from the unknown samples. Details of the analytical conditions are given in Table S1. Isoplot 4.15 (Ludwig, 2012) was used to create concordia diagrams and calculation of a weighted mean age.

In order to obtain accurate crystallization ages for young (<2 Ma) zircon, it is necessary to consider the contributions of common Pb and initial disequilibrium caused by Th/U and Pa/U fractionation in the zircon-melt system (Sakata et al., 2017; Sakata, 2018). We performed the correction for common Pb by a single correction based on a modified Tera-Wasserburg concordia diagram (modified ^{207}Pb method; Sakata, 2018). In order to confirm the initial disequilibrium on the zircon data obtained in this study, we also made correction of the initial disequilibrium effect and compared it with the equilibrium results. For the initial disequilibrium correction, we used the average Th/U ratio of analyzed zircon (0.67) for the Th/U ratio of zircon grains at the time of zircon crystallization [$(Th/U)_{Zircon}$]. Th/U ratio of the melt [$(Th/U)_{Melt}$] was assumed to be 4.8, which was an average derived from river sand samples collected in the vicinity of the Kurobegawa Granite (Imai et al., 2004; Ito et al., 2013). Then, we used a Th/U fractionation factor [$f_{Th/U} = (Th/U)_{Zircon}/(Th/U)_{Melt}$] of 0.123 with 30% of estimation error for the initial Th/U fractionation correction. In this study, we assumingly used general value of Pa/U fractionation factor between melt and zircon [$f_{Pa/U}$= $(Pa/U)_{Zircon}/(Pa/U)_{Melt}$] of 3.36 with 30% of estimation error (compilation value based on Rioux et al., 2015; Sakata et al., 2017; Schmitt, 2011), because we did not determine a Pa/U partitioning factor.)

4 Sample description

Two unweathered samples of the Shiaidani Granodiorite (Harayama, 2015) were collected from the outcrop exposures (Figure 1). These samples are likely affected by post-magmatic hydrothermal activity as indicated by complex patchy chemical zoning of amphibole, chloritization of biotite and partial sericitization of plagioclase. In order to check coexistence of mineral phases required for the application of the Al-in-hornblende geobarometry, a detailed mineral description is made for these samples.

Sample KRG16-07 is a hornblende-biotite granite (Figure 2), which was collected at the same outcrop as KRG-07 showing U-Pb zircon age of 5.6 ± 0.1 Ma (Ito et al., 2013). Matrix mineral assemblage of this sample is amphibole + biotite (mostly chloritized) + plagioclase + quartz + K-feldspar + magnetite + titanite + zircon + apatite + allanite. Amphibole shows gradual core/rim chemical zoning accompanied by discontinuous patchy replacements; the core and patchy replacements are dark under the back scattered electron (BSE) images whereas the rim is slightly bright under the BSE images (Figure 2c). The core is weakly enriched in Mg (Figure 2f) and Na

(Figure 2h), while the rim is weakly enriched in Fe (Figure 2d) and K (Figure 2k). The patchy replacements are enriched in Mg (Figure 2f), Mn and Si, and depleted in Fe (Figure 2d), Al (Figure 2e), Cl (Figure 2g), Na (Figure 2h) and K (Figure 2k) compared to the core. The amphibole is mostly magnesiohornblende except for the final-stage rim and patches corresponding to actinolite (Figure 3). The amphibole core and rim enclose biotite, K-feldspar, plagioclase, ilmenite, magnetite, zircon and apatite. On the other hand, the patchy replacements include biotite (partly chloritized), plagioclase, titanite, K-feldspar, magnetite, zircon and apatite. Oscillatory-zoned plagioclase shows a decrease in anorthite content at the rim, and the plagioclase rim in contact with hornblende rim shows composition of An14-22. An albitic outermost rim (<An14) is locally developed on the An14-22 plagioclase, and such plagioclase is commonly in contact with patchy replacements. The composition of albitic plagioclase enclosed in the patchy replacements is similar to the composition of the outermost albitic rim of matrix plagioclase (Figure 2e, i).

Sample KRG16-101 is a hornblende-biotite granite (Figure 4). Matrix mineral assemblage is amphibole + biotite + plagioclase + quartz + K-feldspar + magnetite + titanite + zircon + apatite + allanite. Chloritization of biotite is weaker compared to sample KRG 16-07, and is only limited to the rims and along the cleavages of biotite. Amphibole shows core/rim chemical zoning with patchy zoning under BSE images. The gradual core/rim zoning is recognized as darker core with brighter rim under the BSE images (Figure 4c). The discontinuous, commonly BSE-dark patchy replacements cut the gradual zoning pattern. The rim is enriched in Fe (Figure 4e), Na (Figure 4i), K (Figure 4l) and Mn, and depleted in Mg (Figure 4g) compared to the core. The BSE-dark patchy replacements are more depleted in Mg (Figure 4g), Al (Figure 4f), Cl (Figure 4h) and Na (Figure 4i), and enriched in Si (Figure 4d) and Mn as observed by X-ray chemical mappings. The amphibole is mostly magnesiohornblende except for the final-stage patchy replacements that correspond to actinolite (Figure 5). The amphibole core and rim include plagioclase (rim with An18), K-feldspar, quartz, magnetite, ilmenite, apatite, zircon whereas the patchy replacements include albitic plagioclase, K-feldspar, quartz, chloritized biotite, magnetite, titanite, apatite, zircon. Composite pseudo-inclusion of K-feldspar and albitic plagioclase, which is connected with matrix via cracks, is commonly developed even in the core of amphibole. Oscillatory-zoned plagioclase in the matrix shows decrease in anorthite content at the rim, and the composition of the rim in contact with amphibole rim is An14-26. Locally, albitic film (<An14) is developed at the plagioclase rim. On the other hand, amphibole is enclosed in plagioclase showing various compositions of An39-52, An39-41 (core) and An16-17 (rim).

5 U-Pb zircon dating of KRG16-101

Zircons in this sample is commonly euhedral, and present in the matrix and also enclosed in biotite, hornblende, quartz and K-feldspar. It is oscillatory- and sector-zoned under CL images (Figure 6, inset). Mineral inclusions such as apatite are common in zircon. Th/U ratio of oscillatory-zoned rim ranges from 0.42 to 1.08 (0.65 in average). Dates of oscillatory-zoned rims are determined for sample KRG16-101, and the results are summarized in Table S2. Concordia plots with 1σ error ellipses show that the analytical results not corrected for the contribution of the common Pb and initial disequilibria are discordant (Figure 6). Common Pb-corrected weighted average of the 24 analysis spots yielded ^{238}U-^{206}Pb age of 5.20 ±0.17 Ma (95% confidence level, MSWD = 0.27, probability = 0.999). The initial disequilibrium correction resulted in ~2% difference in the weighted average age, *i.e.*, 5.31 ±0.17 Ma (95% confidence level, MSWD = 0.27, probability = 1.000). For simplicity, we prefer the former age assuming initial equilibrium in this study.

6 Amphibole composition and application of Al-in-hornblende geobarometry

The chemical composition of amphiboles in sample KRG 16-07 is plotted in Figure 3 and that in sample KRG16-101 is plotted in Figure 5. As described above, amphibole represents gradual chemical zoning from the core to the rim, and discontinuous patchy replacements cut this texture (Figures 3 and 5). In creating Figures 3 and 5, the cores, rims and replacements are classified based mainly on BSE images and partly on X-ray mappings. Therefore, discrimination between gradual core and rim was not always easy under the BSE images alone, and caused scattering of core points within rim-dominant compositional areas (Si > ~7.1 a.p.f.u. and Al_{IV} < ~0.9 a.p.f.u. areas of Figures 3 and 5). Nevertheless, it is important that original core/rim zoning and discontinuous patchy replacements are chemically discriminated at around Si = 7.3 a.p.f.u. and Al_{IV} = 0.7 a.p.f.u. (O = 23) for both samples (Figures 3 and 5).

Because patchy replacements include secondary minerals such as albitic plagioclase, chloritized biotite, and composite pseudo-inclusion of K-feldspar and albitic plagioclase that is connected with matrix via cracks (Figures 2 and 4; note inclusion minerals in Al-poor patches), it is considered that the patchy replacements are the recrystallized domains during hydrothermal alteration. The most extensive amphibole composition that patchy replacements show is actinolitic composition (Figures 3 and 5), and coexistence of such domains with albitic plagioclase and chloritized biotite also supports the alteration under subsolidus hydrothermal condition.

On the other hand, amphibole domains that show original core/rim zoning preserve amphibole composition of igneous stage as supported by presence of more calcic plagioclase inclusions (~An18) as well as higher Al contents of the amphibole domains compared to the replacements. The mineral inclusions in the igneous amphibole domains (plagioclase, K-feldspar, quartz, magnetite, ilmenite, apatite) and the matrix minerals in contact with amphibole rim (biotite, plagioclase rim) satisfy the mineral assemblage required for the application of Al-in-hornblende geobarometer (Mutch et al., 2016). Therefore, Al-in-hornblende geobarometer is applied to the amphibole rim to constrain the solidification pressure of the granite. Hornblende-plagioclase geothermometer (Holland & Blundy, 1994) is also applied to the amphibole rim and plagioclase rim in contact with the amphibole rim. Composition of amphibole rim enclosed in plagioclase rim is also used for the *P-T* estimate (Figure 7). Although *P-T* estimates from patchy replacement is not considered to represent the solidification condition, they are also plotted in Figure 7 for comparison. The Mutch et al. (2016) calibration is preferred in this study, because it is experimentally calibrated for pressure down to 0.8 kbar and applicable to shallower plutons without extrapolation compared to previous calibrations (e.g., 2.5-13 kbar for Schmidt, 1992). Additionally, calibration dataset of Mutch et al. (2016) involves very wide range of plagioclase composition (An15-76), and applicable without extrapolation to the mineral assemblage with low-An plagioclase (≧An15) as in the case of the studied samples.

Application of the Al-in-hornblende geobarometer (Mutch et al., 2016) and hornblende-plagioclase geothermometer (Holland & Blundy, 1994) to the amphibole rim and plagioclase rim pair resulted in 616-691℃ and 0.17-0.27 GPa (±0.04 GPa) for KRG 16-07, and 620-702℃ and 0.17-0.29 GPa (±0.05 GPa) for KRG16-101 (Figure 7). These *P-T* estimates are plotted on the haplogranite solidus within error (Figure 7). Assuming rock density of 2700 kg/m^3 and lithostatic pressure gives solidification depths of 6.3 ±1.0 km to 10.3 ±1.7 km for KRG 16-07, and 6.4 ±1.0 km to 11.0 ±1.8 km for KRG 16-101.

7 Discussion

7.1 Discriminating magmatic and hydrothermally recrystallized amphibole

The Kurobe area exposes younger granite of ca. 0.8 Ma (Ito et al., 2013; 2017; Spencer et al., 2019), and estimation of denudation rate by low-temperature geochronology can be thermally affected by younger intrusions. On the other hand, estimation of exhumation rate based on Al-in-hornblende geobarometry is not strongly affected by later intrusions if the post crystallization, hydrothermal recrystallization of amphibole can be properly evaluated. The exhumation rate can be considered as the lowest estimate of an average denudation rate of the area, because denudation takes into account the lateral movement of the exhumed rocks (Batt & Braun, 1999; Ring et al., 1999; Reiners & Brandon, 2006; Sueoka & Tagami, 2019).

Chivas (1981) proposed that amphiboles with Si > 7.3 a.p.f.u. (Al_{IV} < 0.7 a.p.f.u.) are not truly magmatic and crystallized under subsolidus conditions in the presence of a fluid phase. In this study, chemical boundary between rim and discontinuous patchy replacements of amphibole, determined based on microtextural observation, is recognized at Si = 7.3 a.p.f.u. and Al_{IV} = 0.7 a.p.f.u. (Figures 3 and 5). The patchy replacements commonly enclose and coexist with albitic plagioclase and chloritized biotite, which is consistent with the interpretation of Chivas (1981) that it is the recrystallized domain under subsolidus conditions in the presence of a fluid phase. Some of the *P-T* conditions estimated using the patchy replacements and the plagioclase composition in contact with them are plotted away from the haplogranite solidus (Figure 7), supporting the subsolidus origin of patchy replacements. Therefore, criterion of Chivas (1981) is applicable to the Shiaidani Granodiorite as well, and patchy replacements should not be used in estimating the solidification pressure of the granite, although some of the patches yield pressure similar to that obtained from the magmatic amphibole rim (Figure 7).

7.2 Estimating the lower limit of the average denudation rate of the Shiaidani Granodiorite area after ca. 5.6-5.2 Ma

The presence of magmatic oscillatory zoning and absence of secondary replacement microtextures in the dated zircon grains (Figure 6a inset) suggests that the U-Pb zircon ages of ca. 5.6-5.2 Ma can be interpreted as the crystallization ages of these samples. By dividing the estimated solidification depths by the U-Pb zircon age, average exhumation rate of the Shiaidani Granodiorite is estimated as 0.93-2.2 mm/yr from KRG 16-07 and 1.0-2.5 mm/yr from KRG 16-101. This is considered to be the lowest estimate of the average denudation rate since ca. 5.6-5.2 Ma for the area where the Shiaidani Granodiorite is exposed. Nonetheless, uplift and denudation in the northern Hida Range, including the Kurobe area, could be accelerated since ca. 1.5-1.0 Ma, considering depositional ages of granitic gravels sourced from the Hida Range to the Matsumoto basin to the east (Oikawa & Wada, 2004). The estimation in this study may provide the lower limit of the denudation rates since ca. 1.5-1.0 Ma, considering the higher denudation rates (several to 10 mm/yr at a maximum) in shorter timescales estimated based on the sedimentary yields in catchments (Ohmori, 1978; Fujiwara et al., 1999) and terrestrial *in-situ* cosmogenic nuclide techniques (Matsushi et al., 2014).

8 Conclusion

We estimated the solidification depth of the Shiaidani Granodiorite utilizing Al-in-hornblende geobarometry and solidification age using U-Pb zircon dating. The Al-poor patchy replacements developed in amphiboles are probably hydrothermally recrystallized domains and should not be used for solidification pressure estimates. The lower limit of an average denudation rate after ca. 5.6-5.2 Ma for the area where Shiaidani Granodiorite is exposed is estimated as 0.93-2.5 mm/yr.

Acknowledgement

We would like to thank Dr. Hisatoshi Ito and an anonymous reviewer for constructive comments, and Prof. Tomokazu Hokada and Prof. Tatsuki Tsujimori for editorial efforts. This study was funded by the Ministry of Economy, Trade and Industry (METI), Japan as part of its R&D supporting program titled “Establishment of Advanced Technology for Evaluating the Long-term Geosphere Stability on Geological Disposal Project of Radioactive Waste (Fiscal Years 2018 and 2020)”. This work was also supported by the Grant-in-Aid for Scientific Research on Innovative Areas (KAKENHI No. 26109003) from the Ministry of Education, Culture, Sports, Science and Technology (MEXT). The mineral separation was performed by Dr. Tohru Danhara and Dr. Hideki Iwano (Kyoto Fission-Track Co., Ltd.). The field survey was supported by Dr. Tetsuya Komatsu, Shuji Terusawa (JAEA), Shoma Fukuda, Takayuki Arai (Kyoto University), Yasuhisa Hino (KANSO Co., Ltd.), and staffs of the Azohara Onsengoya, Senninike Hutte, and Kansai Electric Power Co., Inc. TK thanks Kota Suzuki and Ayu Yamazaki (Kyoto University) for discussion. GEK acknowledges financial support for sample collection from a Mobility Grant from the University of Cologne and Swiss National Science Foundation (SNSF) grant number PZ00P2_167960.

ORCID IDs

Tetsuo Kawakami, https://orcid.org/0000-0002-5921-5562

Shigeru Sueoka, https://orcid.org/0000-0002-5264-2713

Tatsunori Yokoyama, https://orcid.org/0000-0003-0667-6207

Saya Kagami, https://orcid.org/0000-0001-5704-079X

Georgina E. King, https://orcid.org/0000-0003-1059-8192

Frédéric Herman, https://orcid.org/0000-0002-7237-4656

Sumiko Tsukamoto, https://orcid.org/0000-0003-4626-4784

Takahiro Tagami, https://orcid.org/0000-0002-4209-5541

References

Anderson. J.L., & Smith, D.R. (1995). The effects of temperature and fO_2 on the Al-in-hornblende barometer. American Mineralogist, 80, 549-559.

Batt, G.E., & Braun, J. (1999). The tectonic evolution of the Southern Alps, New Zealand: Insights from fully thermally coupled dynamical modelling. Geophysical Journal International, 136, 403-420.

Chivas, A.R. (1981). Geochemical evidence for magmatic fluids in porphyry copper mineralization. Part I. Mafic silicates from the Koloula Igneous Complex. Contribution to Mineralogy and Petrology, 78, 389-403.

Fujiwara, O., Sanga, T., & Ohmori, H. (1999). Regional distribution of erosion rates over the Japanese Islands. Japan Nuclear Cycle Technical Review, 5, 85–93 (in Japanese with English abstract).

Hammarstrom, J.M., & Zen, E-an. (1986). Aluminum in hornblende: An empirical igneous geobarometer. American Mineralogist, 71, 1297-1313.

Hartung, E., Caricchi, L., Floess, D., Wallis, S., Harayama, S., Kouzmanov, K., & Chiaradia, M. (2017). Evidence for Residual Melt Extraction in the Takidani Pluton, Central Japan. Journal of Petrology, 58, 763–788.

Harayama, S. (2015). Vertically turned Quaternary collapsed caldera and Kurobegawa Granite complex, exposed around the Mt. Kashimayari and Mt. Jii, Northern Japan Alps: The Journal of the Geological Society of Japan, 121, 293–308 (in Japanese).

Harayama, S., Takahashi, M., Shukukawa, R., Itaya, T., & Yagi, K. (2010). High-temperature hot springs and Quaternary Kurobegawa Granite along the Kurobegawa River. Journal of Geological Society of Japan, 116, Supplement, 63–81 (in Japanese).

Holland, T., & Blundy, J. (1994). Non-ideal interactions in calcic amphiboles and their bearing on amphibole-plagioclase thermometry. Contributions to Mineralogy and Petrology, 116, 433-447.

Imai, N., Terashima, S., Ohta, A., Mikoshiba, M., Okai, T., Tachibana, Y., Togashi, S., Matsuhisa, Y., Kanai, Y., Kamioka, H., & Taniguchi, M. (2004). Geochemical map of Japan. Geological Survey of Japan, AIST, 209p.

Ito, H., Yamada, R., Tamura, A., Arai, S., Horie, K., & Hokada, T. (2013). Earth's youngest exposed granite and its tectonic implications: the 10–0.8 Ma Kurobegawa Granite. Scientific Reports, 3, 1306, https://doi.org/10.1038/srep01306

Ito, H., Spencer, C.J., Danišík, M., & Hoiland, C.W. (2017). Magmatic tempo of Earth's youngest exposed plutons as revealed by detrital zircon U-Pb geochronology. Scientific Reports, 7, 12457, https://doi.org/10.1038/s41598-017-12790-w

Iwano H., Orihashi Y., Hirata T., Ogasawara, M., Danhara, T., Horie, K., Hasebe, N., Sueoka, S., Tamura, A., Hayasaka, Y., Katsube, A., Ito, H., Tani, K., Kimura, J.-I., Chang, Q., Kouchi, Y., Haruta, Y., & Yamamoto, K. (2013). An interlaboratory evaluation of OD-3 zircon for use as a secondary U–Pb dating standard. Island Arc 22, 382–394.

Johannes, W., & Holtz, W. (1996). Petrogenesis and Experimental Petrology of Granitic Rocks. Springer-Verlag, Berlin Heidelberg.

Ludwig, K., (2012). User’s manual for Isoplot version 3.75–4.15: a geochronological toolkit for Microsoft Excel. Berkley Geochronological Center Special Publication 5.

Matsushi, Y., Matsuzaki, H., & Chigira, M. (2014). Determining long-term sediment yield from mountainous watersheds by terrestrial cosmogenic nuclides. Journal of the Japan Society of Engineering Geology, 54, 272-280. (in Japanese with English abstract)

Mutch, E.J.F., Blundy, J.D., Tattitch, B.C., Cooper, F.J., & Brooker, R.A. (2016). An experimental study of amphibole stability in low-pressure granitic magmas and a revised Al-in-hornblende geobarometer. Contributions to Mineralogy and Petrology, 171, 85. https://doi.org/10.1007/s00410-016-1298-9

Ogata, S., Miyakoshi, K., Shidahara, T., & Tanaka, K. (1983). Geology of the Kurobe geothermal area. Central Research Institute of Electric Power Industry Report, 382032, 27p. (in Japanese with English abstract)

Ohmori, H. (1978). Relief structure of the Japanese mountains and their stages geomorphic development. Bulletin of the Department of Geography, University of Tokyo, 10, 31-83.

Oikawa, T., & Wada, H. (2004). Rapid uplifting in the northern part of Hida Mountain Range at 1 Ma, based on lithofacies and petrography in the Iyari Formation. Journal of the Geological Society of Japan, 110, 528-535. (in Japanese with English abstract)

Reiners, P.W., & Brandon, M.T. (2006). Using thermochronology to understand orogenic erosion. Annual Review of Earth and Planetary Science, 34, 419-466. https://doi.org/10.1146/annurev.earth.34.031405.125202

Ring, U., Brandon, M.T., Willett, S.D., & Lister, G.S. (1999) Exhumation processes. Geological Society, London, Special Publications, 154, 1-27.

Rioux, M., Bowring, S., Cheadle, M., & John, B. (2015). Evidence for initial excess ^{231}Pa in mid-ocean ridge zircons. Chemical Geology, 397, 143–156.

Sakata, S., Hirakawa, S., Iwano, H., Danhara, T., Guillong, M., & Hirata, T. (2017). A new approach for constraining the magnitude of initial disequilibrium in Quaternary zircons by coupled uranium and thorium decay series dating, Quaternary Geochronology, 38, 1-12.

Sakata, S. (2018). A practical method for calculating the U-Pb age of Quaternary zircon: Correction for common Pb and initial disequilibria. Geochemical Journal, 52, 281–286.

Schmitt, A.K. (2011). Uranium series accessory crystal dating of magmatic processes. Annual Review of Earth and Planetary Sciences, 39, 321–349.

Schmidt, M.W. (1992). Amphibole composition in tonalite as a function of pressure: an experimental calibration of the Al-in-hornblende barometer. Contributions to Mineralogy and Petrology, 110, 304-310.

Spencer, C.J., Danišík, M., Ito, H., Hoiland, C., Tapster, S., Jeon, H., McDonald, B., & Evans, N.J. (2019). Rapid Exhumation of Earth's Youngest Exposed Granites Driven by Subduction of an Oceanic Arc. Geophysical Research Letters, 46, 1259-1267.

Sueoka, S., & Tagami, T. (2019). Low-temperature thermochronology and its application to tectonics in the shallow crust. Journal of Geography (Chigaku Zasshi), 128, 707-730.

Wiedenbeck, M., Alle, P., Corfu, F., Griffin, W.L., Meier, M., Oberli, F., Vob Quadt, A., Roddick, J.C., & Spiegel, W. (1995). Three natural zircon standards for U–Th–Pb, Lu–Hf, trace element and REE analyses. Geostandards Newsletter, 19, 1–23.

Wiedenbeck, M., Hanchar, J.M., Peck, W.H., Sylvester, P., Valley, J., et al. (2004). Further characterisation of the 91500 zircon crystal. Geostandards and Geoanalytical Research, 28, 9–39.

Yamada, R. (1997). Fission Track Thermochronology: Thermal Characteristics of Fission Tracks in Zircon, and Cooling History Analysis of the Granitic Bodies around the Northern Alps, Central Japan. 128p. Kyoto University doctoral dissertation. https://doi.org/10.11501/3123276

Yamada, R., & Harayama, S. (1999). Fission track and K-Ar dating on some granitic rocks of the Hida mountain range, Central Japan. Geochemical Journal, 33, 59-66.

Yamaguchi, Y., Wada, H., Ohta, Y., & Harayama, S. (2003). Amphibole zoning, a record of progressive oxidation during crystallization of mafic microgranular enclaves in the Kurobegawa granitic pluton. Journal of Mineralogical and Petrological Sciences, 98, 151-155.

Figure captions

Figure 1 Simplified geological map of the Kurobe area modified after Harayama et al. (2010) and Harayama (2015). Sample localities are also shown. The approximate emplacement ages (Ma) are indicated by the subscript numbers attached to F, G and V following Harayama (2015). MTL: Median Tectonic Line, ISTL: Itoigawa-Shizuoka Tectonic Line.

Figure 2 Photomicrographs, back scattered electron (BSE) image and X-ray elemental maps of an amphibole in sample KRG 16-07. (a) Photomicrograph of an amphibole-bearing domain. Plane polarized light (PPL). (b) Crossed polarized light (CPL) of (a). (c) BSE image of the same area as (a) and (b). White square represents the area for the X-ray elemental mapping shown in (d)-(k). (d)-(k) X-ray elemental maps for (d) Fe, (e) Al, (f) Mg, (g) Cl, (h) Na, (i) Ca, (j) Ti and (k) K. Note that albitic plagioclase and chloritized biotite are enclosed in Al-poor patchy replacements. Amp: amphibole, An: anorthite, Ap: apatite, Bt: biotite, Chl: chlorite, Ilm: ilmenite, Kfs: K-feldspar, Mag: magnetite, Pl: plagioclase, Qtz: quartz, Ttn: titanite.

Figure 3 Chemical composition of amphibole (O = 23) in sample KRG 16-07. (a) (Na+K) in A-site vs

Si, (b) Cl vs Al_{IV}, (c) $Mg/(Mg+Fe^{2+})$ vs Si, (d) $Mg/(Mg+Fe^{2+})$ vs Al_{IV}. Solid black lines represent compositional boundaries of amphiboles. Blue broken lines represent Si = 7.3 a.p.f.u. and Al_{IV} = 0.7 a.p.f.u.

Figure 4 Photomicrographs, BSE image and X-ray elemental maps of an amphibole in sample KRG 16-101. (a) Photomicrograph of an amphibole-bearing domain. PPL. (b) CPL photo of (a). (c) BSE image of the boxed area in (b). (d)-(k) X-ray elemental maps for the boxed area in terms of (d) Si, (e) Fe, (f) Al, (g) Mg, (h) Cl, (i) Na, (j) Ca, (k) Ti and (l) K. Note that albitic plagioclase and chloritized biotite are enclosed in Al-poor patchy replacements.

Figure 5 Chemical composition of amphibole (O = 23) in sample KRG 16-101. (a) (Na+K) in A-site vs Si, (b) Cl vs Al_{IV}, (c) $Mg/(Mg+Fe^{2+})$ vs Si, (d) $Mg/(Mg+Fe^{2+})$ vs Al_{IV}. Solid black lines represent compositional boundaries of amphiboles. Blue broken lines represent Si = 7.3 a.p.f.u. and Al_{IV} = 0.7 a.p.f.u.

Figure 6 (a) Conventional (Wetherill) and (b) Tera–Wasserburg concordia diagrams for U-Pb zircon dating of KRG 16-101. Inset in (a) is an example of CL image of a dated zircon grain (spot KRG 16-101-09).

Figure 7 *P*-*T* diagrams showing the estimated solidification conditions for (a) KRG 16-07 and (b) KRG 16-101. A water-saturated haplogranite solidus line is from Johannes and Holtz (1996).

Table S1 Instrumentation and operational settings for LA−ICP−MS analysis.

Table S2 (a) Results of LA−ICP−MS U−Pb zircon dating with common Pb correction assuming initial equilibrium. (b) Results of LA−ICP−MS U−Pb zircon dating with common Pb correction assuming initial disequilibrium.

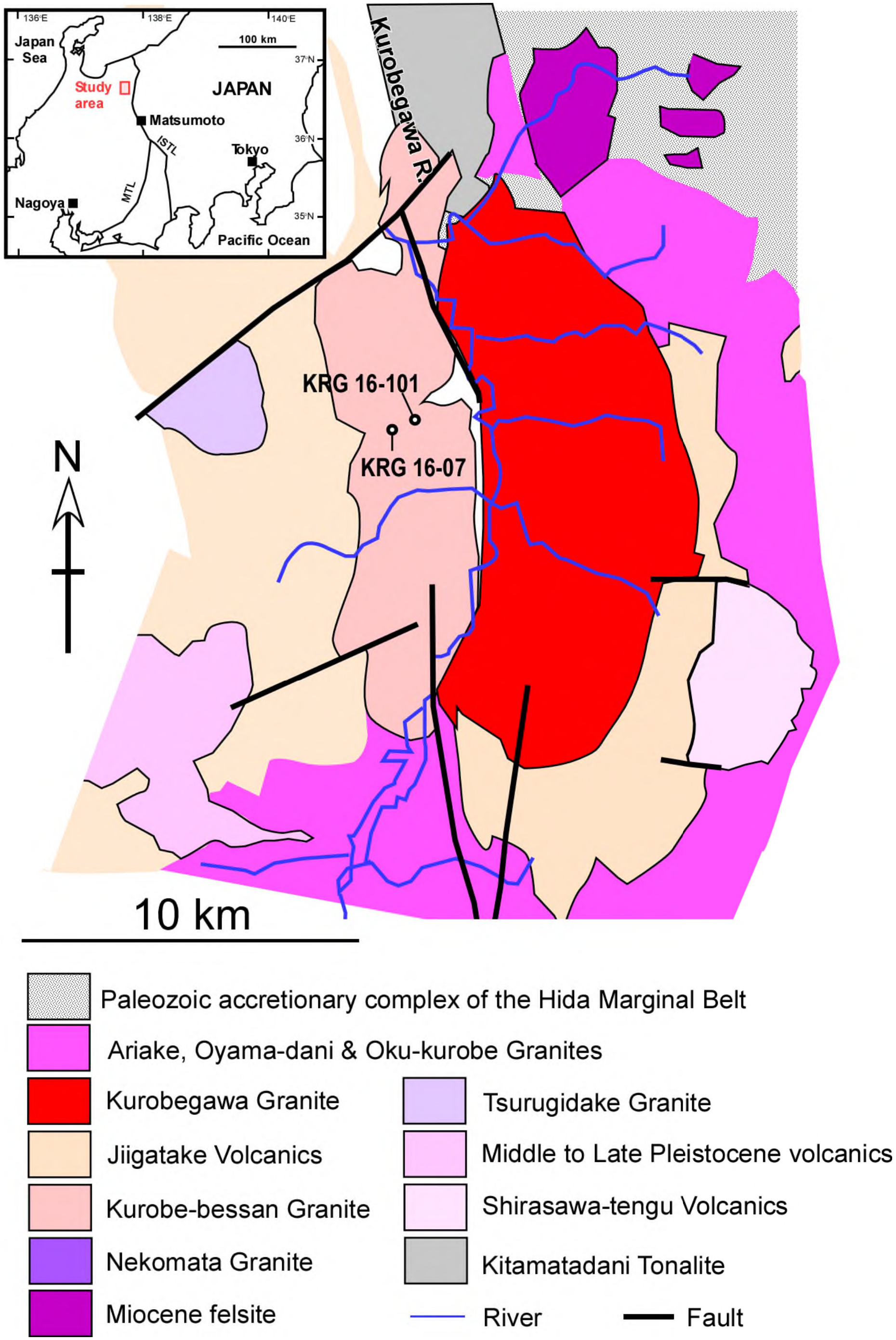

136°E
138°E
140°E
Japan Sea
100 km
37°N
Study area
JAPAN
Matsumoto
36°N
ISTL
Tokyo
MTL
Nagoya
35°N
Pacific Ocean
Kurobegawa R.
KRG 16-101
KRG 16-07
N
10 km
Paleozoic accretionary complex of the Hida Marginal Belt
Ariake, Oyama-dani & Oku-kurobe Granites
Kurobegawa Granite
Jiigatake Volcanics
Kurobe-bessan Granite
Nekomata Granite
Miocene felsite
Tsurugidake Granite
Middle to Late Pleistocene volcanics
Shirasawa-tengu Volcanics
Kitamatadani Tonalite
River
Fault

Fig. 1

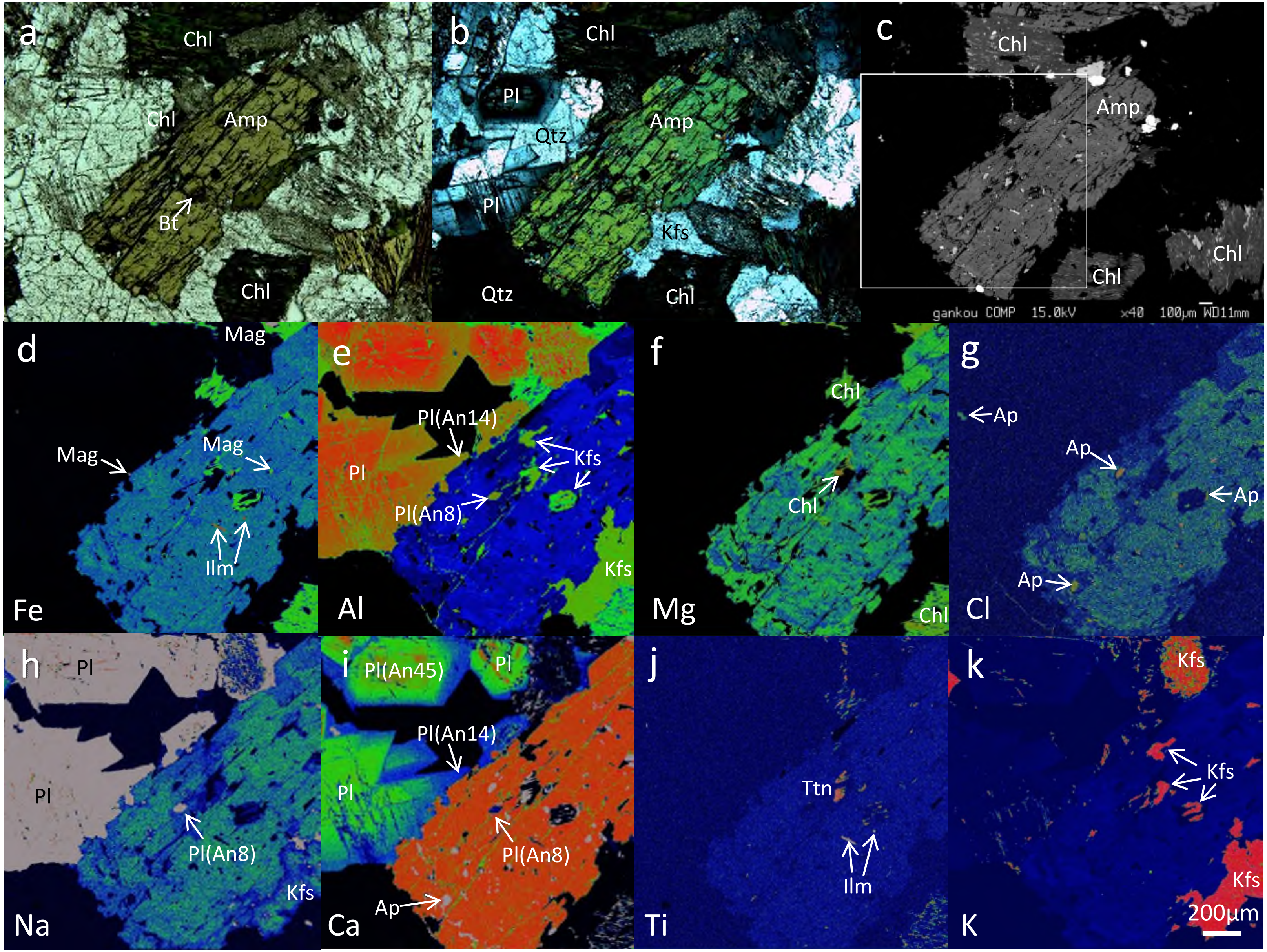

a
Chl
Chl
Amp
Bt
Chl
b
Chl
Pl
Qtz
Amp
Pl
Kfs
Qtz
Chl
c
Chl
Amp
Chl
Chl
gankou COMP 15.0kV x40 100µm WD11mm
d
Mag
Mag
Mag
Ilm
Fe
e
Pl(An14)
Kfs
Pl
Pl(An8)
Kfs
Al
f
Chl
Chl
Mg
Chl
g
Ap
Ap
Ap
Ap
Cl
h
Pl
Pl
Pl(An8)
Kfs
Na
i
Pl(An45)
Pl
Pl(An14)
Pl
Pl(An8)
Ap
Ca
j
Ttn
Ilm
Ti
k
Kfs
Kfs
Kfs
200µm
K

Fig. 2

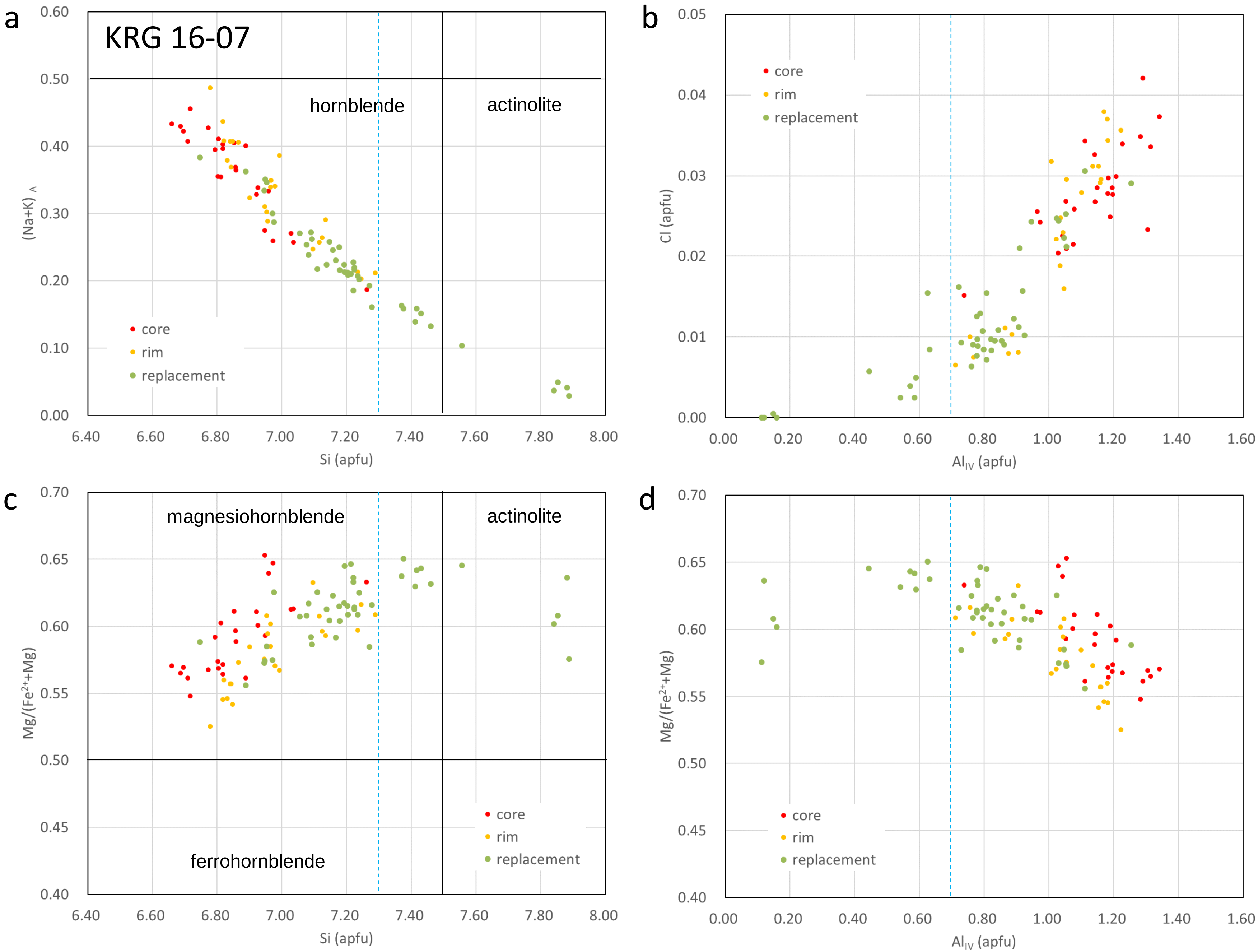
a
KRG 16-07
hornblende
actinolite
core
rim
replacement
(Na+K) A
Si (apfu)
b
core
rim
replacement
Cl (apfu)
Al_{IV} (apfu)
c
magnesiohornblende
actinolite
ferrohornblende
core
rim
replacement
$Mg/(Fe^{2+}+Mg)$
Si (apfu)
d
core
rim
replacement
$Mg/(Fe^{2+}+Mg)$
Al_{IV} (apfu)

Fig. 3

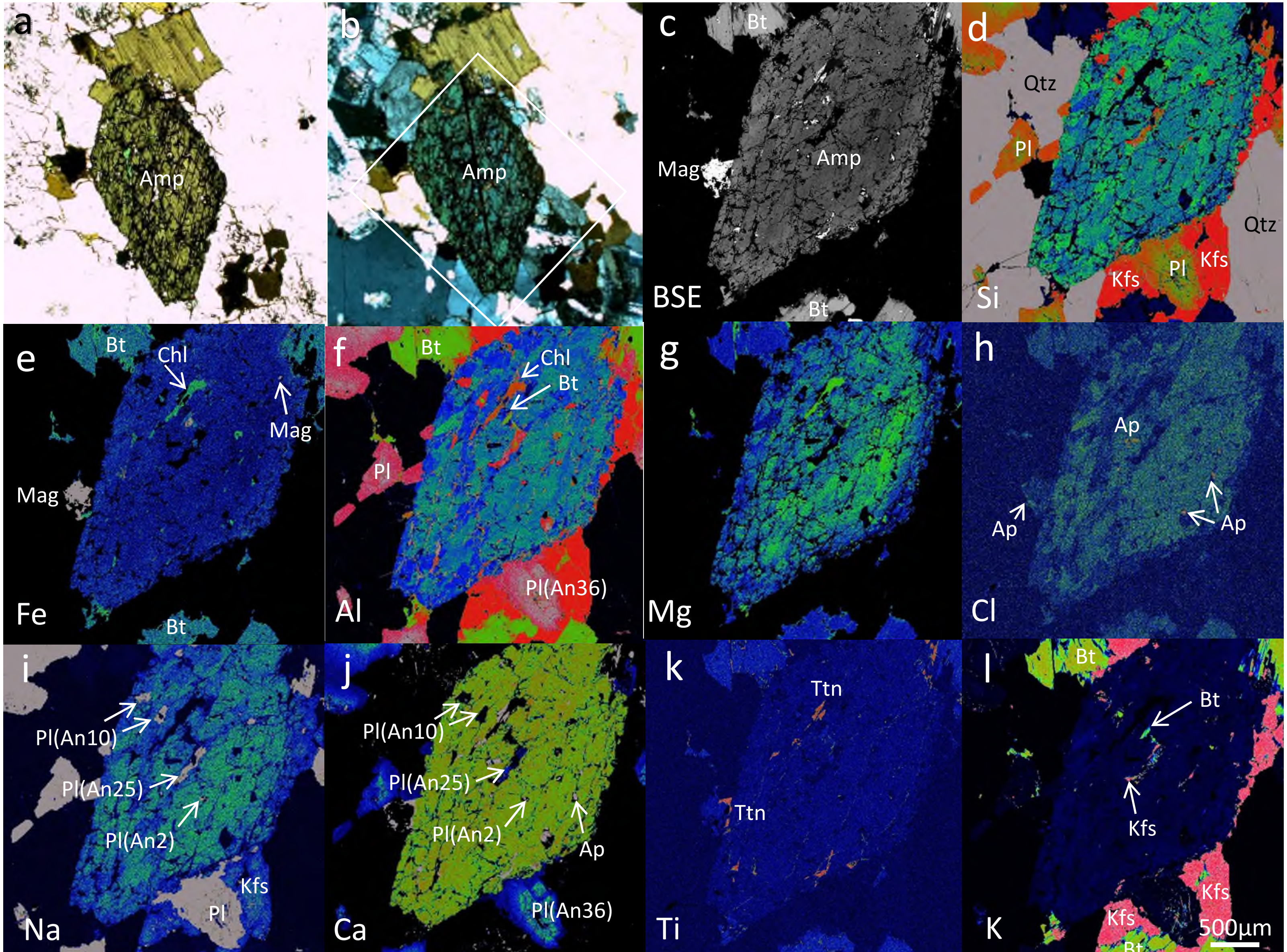
a
Amp
b
Amp
c
Bt
Mag
Amp
BSE
Bt
d
Qtz
Pl
Qtz
Kfs
Pl
Kfs
Si
e
Bt
Chl
Mag
Mag
Fe
Bt
f
Bt
Chl
Bt
Pl
Pl(An36)
Al
g
Mg
h
Ap
Ap
Ap
Cl
i
Pl(An10)
Pl(An25)
Pl(An2)
Kfs
Pl
Na
j
Pl(An10)
Pl(An25)
Pl(An2)
Ap
Pl(An36)
Ca
k
Ttn
Ttn
Ti
l
Bt
Bt
Kfs
Kfs
Kfs
K
500µm
Bt

Fig. 4

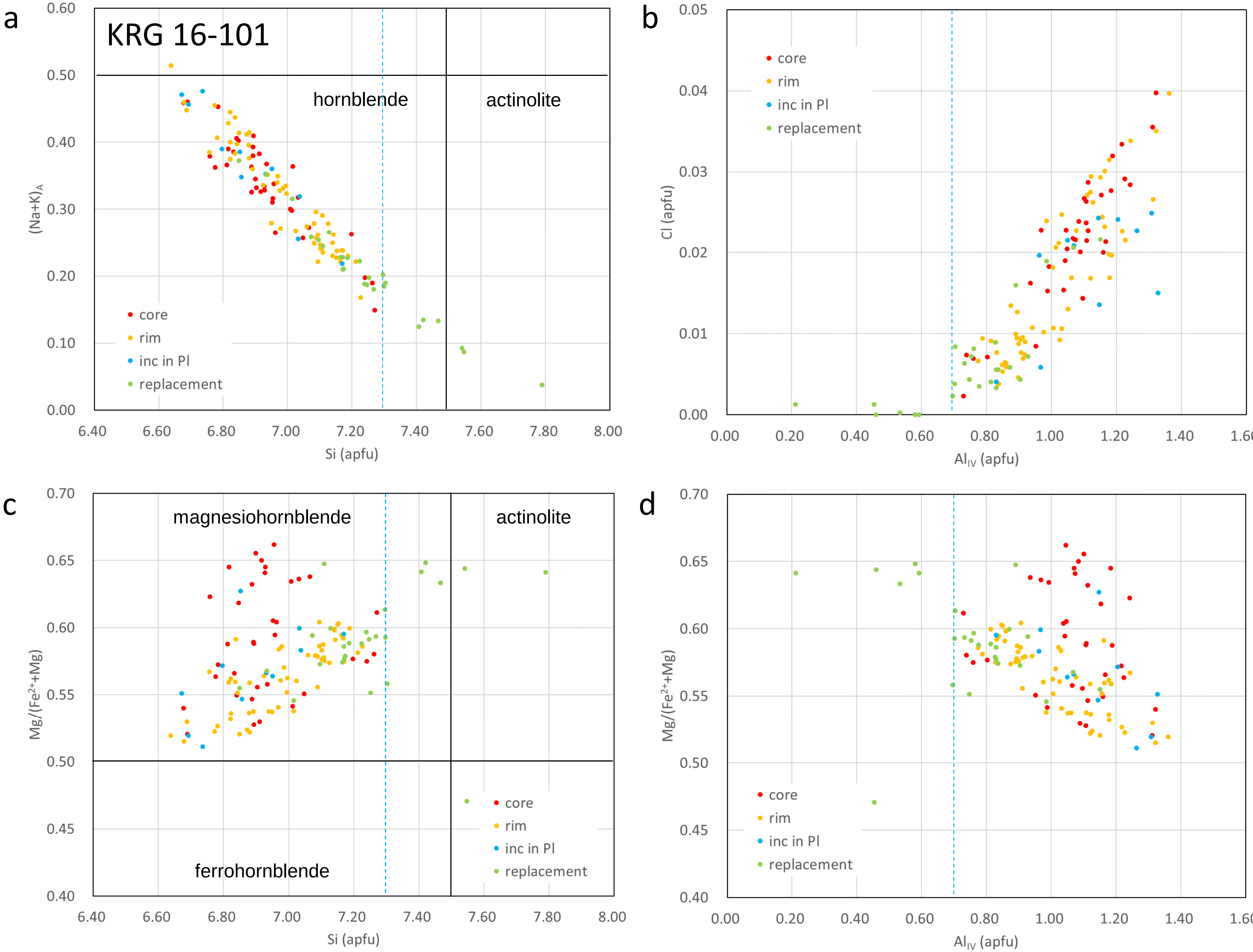
a
KRG 16-101
hornblende
actinolite
core
rim
inc in Pl
replacement
(Na+K)A
Si (apfu)
b
core
rim
inc in Pl
replacement
Cl (apfu)
AlIV (apfu)
c
magnesiohornblende
actinolite
ferrohornblende
core
rim
inc in Pl
replacement
Mg/(Fe2++Mg)
Si (apfu)
d
core
rim
inc in Pl
replacement
Mg/(Fe2++Mg)
AlIV (apfu)
Fig. 5

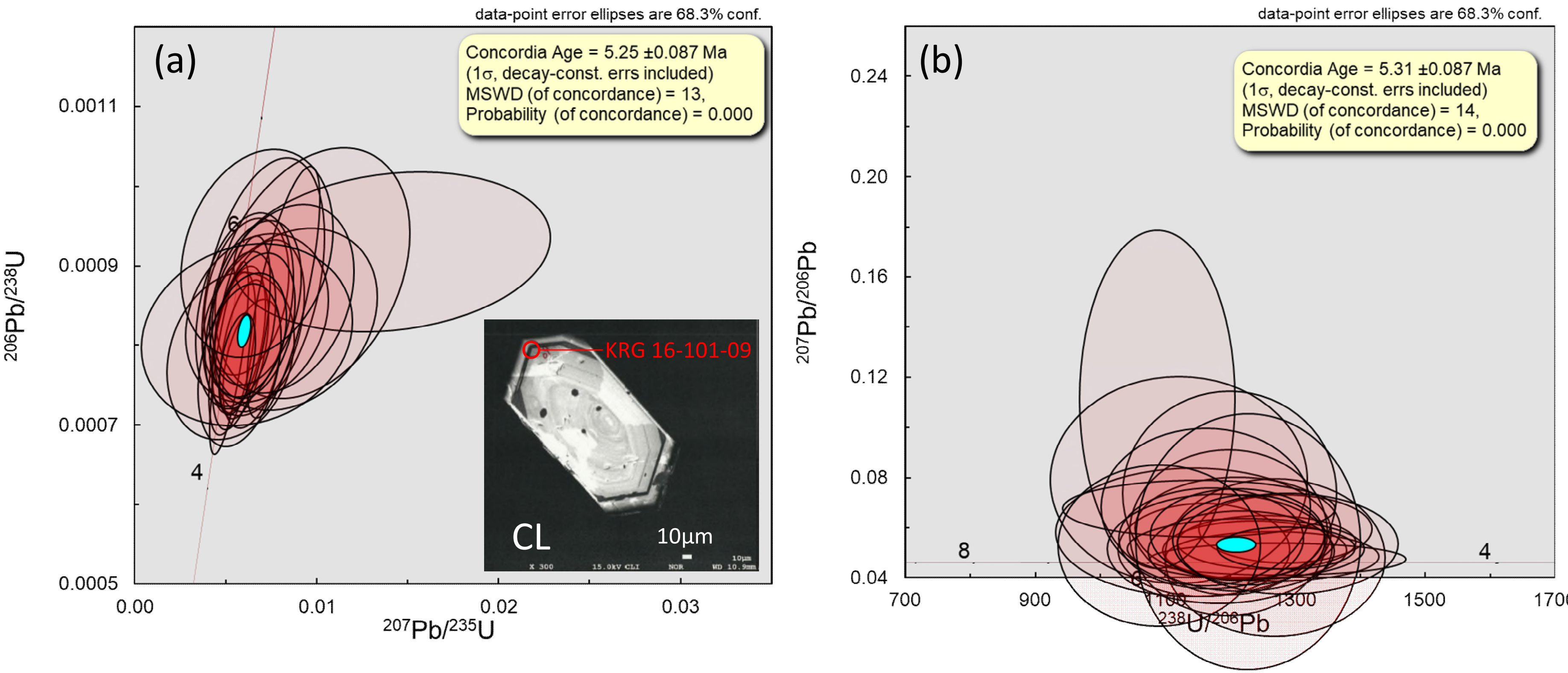
data-point error ellipses are 68.3% conf.
(a)
Concordia Age = 5.25 ±0.087 Ma
(1σ, decay-const. errs included)
MSWD (of concordance) = 13,
Probability (of concordance) = 0.000
0.0011
0.0009
0.0007
0.0005
6
4
$^{206}Pb/^{238}U$
0.00
0.01
0.02
0.03
$^{207}Pb/^{235}U$
KRG 16-101-09
CL
10µm
data-point error ellipses are 68.3% conf.
(b)
Concordia Age = 5.31 ±0.087 Ma
(1σ, decay-const. errs included)
MSWD (of concordance) = 14,
Probability (of concordance) = 0.000
0.24
0.20
0.16
0.12
0.08
0.04
$^{207}Pb/^{206}Pb$
8
4
700
900
1100
1300
1500
1700
$^{238}U/^{206}Pb$

Fig. 6

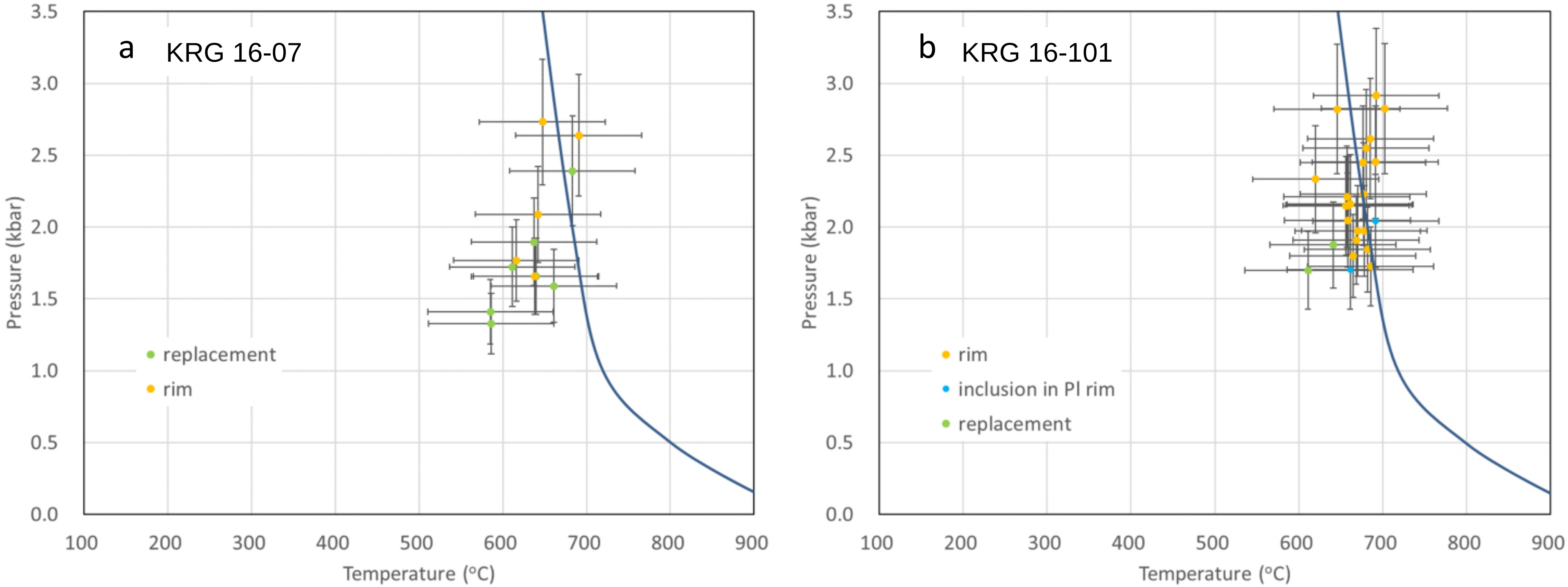
a KRG 16-07
Pressure (kbar)
Temperature (°C)
replacement
rim
b KRG 16-101
rim
inclusion in Pl rim
replacement
3.5
3.0
2.5
2.0
1.5
1.0
0.5
0.0
100
200
300
400
500
600
700
800
900

Fig. 7

Laboratory	JAEA- Toki Geochronology Research Laboratory
Analyst	S. Kagami, T. Yokoyama
Laser ablation system	
Model	Photon-Machines Analyte G2
Laser type	Excimer 193 nm
Energy density	2.0 J cm^{-2}
Crater size	20 µm circle
Repetition rate	10 Hz (200 shots)
Carrier gas	He
He gas flow rate	1.0 L/min
ICP-MS	
Model	Thermo Fisher Scientific Neptune-*Plus*
Forward power	1200 W
Carrier gas	Ar
Ar gas flow rate	1.1 L/min
Scanning mode	Multi-collector Static
Data acquisition protocol	Time resolved analysis
Integration time	0.066s×700 ratios
Monitor isotopes	^{202}Hg (CDD), ^{204}Pb (CDD), ^{206}Pb (SEM), ^{207}Pb (SEM), ^{208}Pb (SEM), ^{232}Th (FC), ^{238}U (FC) *CDD: Compact Discrete Dynode, SEM: Secondary Electron Multiplier, FC: Faraday Cup
Primary standard	91500
Secondary standard	OD-3

Table S2a. Results of LA－ICP－MS U－Pb zircon dating with common Pb correction assuming initial equilibrium.

analysis no.	microtexture	$^{207}Pb/^{235}U$	error (1σ)	$^{206}Pb/^{238}U$	error (1σ)	Error correlation	$^{207}Pb/^{206}Pb$	error (1σ)	common $^{207}Pb/^{206}Pb$	error	$f_{Th/U}$	error (30%)	$f_{Pa/U}$	error (30%)	Common Pb corrected age (Ma)	error (1σ)	Th (ppm)	U (ppm)	Th/U	* excluded from weighted average
KRG16-101-1	unzoned mantle	8.40462	0.76642	0.07334	0.00608	0.90954	0.83109	0.03150	0.83594	0	1	0	1	0	456.3	36.6	n.d.	n.d.	n.d.	*
KRG16-101-2	oscillatory-zoned rim	0.00639	0.00106	0.00078	0.00005	0.41295	0.05964	0.00901	0.83594	0	1	0	1	0	4.9	0.3	629	739	0.85	
KRG16-101-3	oscillatory-zoned rim	0.00531	0.00085	0.00079	0.00007	0.53741	0.04874	0.00655	0.83594	0	1	0	1	0	5.1	0.4	600	893	0.67	
KRG16-101-4	oscillatory-zoned rim	0.00568	0.00096	0.00081	0.00006	0.44623	0.05104	0.00774	0.83594	0	1	0	1	0	5.2	0.4	391	674	0.58	
KRG16-101-5	unzoned mantle	0.00610	0.00153	0.00086	0.00006	0.29956	0.05130	0.01231	0.83594	0	1	0	1	0	5.5	0.4	269	379	0.71	
KRG16-101-6	oscillatory-zoned rim	0.02174	0.00997	0.00326	0.00146	0.97558	0.04835	0.00487	0.83594	0	1	0	1	0	20.9	6.5	n.d.	n.d.	n.d.	*
KRG16-101-7	unzoned mantle	0.00597	0.00089	0.00080	0.00006	0.48540	0.05444	0.00707	0.83594	0	1	0	1	0	5.1	0.3	1453	1132	1.28	
KRG16-101-8	unzoned mantle	25.41318	6.34566	0.21903	0.05350	0.97819	0.84149	0.04364	0.83594	0	1	0	1	0	1276.8	289.3	n.d.	n.d.	n.d.	*
KRG16-101-9	oscillatory-zoned rim	0.00515	0.00070	0.00078	0.00008	0.75091	0.04759	0.00427	0.83594	0	1	0	1	0	5.0	0.5	1064	1846	0.58	
KRG16-101-10	unzoned	9.41347	1.10182	0.08136	0.00890	0.93451	0.83913	0.03496	0.83594	0	1	0	1	0	504.2	53.3	n.d.	n.d.	n.d.	*
KRG16-101-11	oscillatory-zoned rim	0.00973	0.00353	0.00089	0.00010	0.32086	0.07917	0.02724	0.83594	0	1	0	1	0	5.5	0.6	404	949	0.43	
KRG16-101-12	oscillatory-zoned rim	0.00601	0.00177	0.00084	0.00008	0.32705	0.05166	0.01438	0.83594	0	1	0	1	0	5.4	0.5	169	327	0.52	
KRG16-101-13	oscillatory-zoned rim	0.00702	0.00222	0.00087	0.00011	0.38820	0.05825	0.01693	0.83594	0	1	0	1	0	5.5	0.6	221	343	0.64	
KRG16-101-14	oscillatory-zoned rim	0.00575	0.00129	0.00082	0.00006	0.34910	0.05082	0.01064	0.83594	0	1	0	1	0	5.3	0.4	317	541	0.59	
KRG16-101-15	oscillatory-zoned rim	0.00523	0.00230	0.00079	0.00007	0.20054	0.04816	0.02073	0.83594	0	1	0	1	0	5.1	0.4	203	221	0.92	
KRG16-101-16	oscillatory-zoned rim	0.00659	0.00165	0.00085	0.00007	0.31936	0.05597	0.01331	0.83594	0	1	0	1	0	5.4	0.4	296	426	0.69	
KRG16-101-17	oscillatory-zoned rim	0.00682	0.00164	0.00082	0.00007	0.35975	0.05997	0.01344	0.83594	0	1	0	1	0	5.2	0.4	321	420	0.76	
KRG16-101-18	oscillatory-zoned rim	0.00811	0.00257	0.00086	0.00008	0.28748	0.06846	0.02080	0.83594	0	1	0	1	0	5.4	0.5	204	256	0.80	
KRG16-101-19	oscillatory-zoned rim, crack	0.00849	0.00317	0.00083	0.00008	0.24292	0.07388	0.02676	0.83594	0	1	0	1	0	5.2	0.5	206	190	1.08	*
KRG16-101-20	oscillatory-zoned rim, crack	0.00654	0.00146	0.00083	0.00006	0.32817	0.05749	0.01211	0.83594	0	1	0	1	0	5.2	0.4	341	461	0.74	*
KRG16-101-21	oscillatory-zoned rim	0.00668	0.00259	0.00083	0.00007	0.21654	0.05806	0.02196	0.83594	0	1	0	1	0	5.3	0.4	116	224	0.52	
KRG16-101-22	oscillatory-zoned rim	0.00558	0.00066	0.00078	0.00004	0.45816	0.05208	0.00550	0.83594	0	1	0	1	0	5.0	0.3	879	1840	0.48	
KRG16-101-23	unzoned rim	0.01410	0.00574	0.00092	0.00007	0.17825	0.11140	0.04459	0.83594	0	1	0	1	0	5.4	0.5	124	254	0.49	
KRG16-101-24	oscillatory-zoned rim	0.00573	0.00151	0.00078	0.00007	0.33107	0.05362	0.01333	0.83594	0	1	0	1	0	4.9	0.4	275	477	0.58	
KRG16-101-25	unzoned	4.92068	0.77426	0.04267	0.00642	0.95639	0.83631	0.03844	0.83594	0	1	0	1	0	269.4	39.8	n.d.	n.d.	n.d.	*
KRG16-101-26	unzoned	8.65497	1.09942	0.07489	0.00879	0.92402	0.83815	0.04071	0.83594	0	1	0	1	0	465.6	52.9	n.d.	n.d.	n.d.	*
KRG16-101-27	unzoned	7.94481	1.06792	0.06892	0.00861	0.92955	0.83603	0.04143	0.83594	0	1	0	1	0	429.7	52.2	n.d.	n.d.	n.d.	*
KRG16-101-28	unzoned	8.76559	1.69260	0.07486	0.01396	0.96585	0.84928	0.04249	0.83594	0	1	0	1	0	465.3	84.3	n.d.	n.d.	n.d.	*
KRG16-101-29	oscillatory-zoned rim	0.00812	0.00132	0.00087	0.00010	0.73813	0.06786	0.00746	0.83594	0	1	0	1	0	5.4	0.6	596	1076	0.55	
KRG16-101-30	oscillatory-zoned rim	0.00669	0.00276	0.00092	0.00009	0.22815	0.05299	0.02129	0.83594	0	1	0	1	0	5.9	0.5	114	195	0.58	
KRG16-101-31	oscillatory-zoned rim	0.03772	0.01384	0.00105	0.00013	0.33810	0.26046	0.08995	0.83594	0	1	0	1	0	4.9	0.9	555	565	0.98	
KRG16-101-32	oscillatory-zoned rim	0.00620	0.00139	0.00081	0.00005	0.28156	0.05527	0.01186	0.83594	0	1	0	1	0	5.2	0.3	340	566	0.60	
KRG16-101-33	unzoned	6.85524	0.64235	0.05887	0.00498	0.90367	0.84459	0.03389	0.83594	0	1	0	1	0	368.7	30.4	n.d.	n.d.	n.d.	*
KRG16-101-34	unzoned, crack	9.95498	1.52518	0.08506	0.01234	0.94689	0.84878	0.04181	0.83594	0	1	0	1	0	526.3	73.7	n.d.	n.d.	n.d.	*
KRG16-101-35	oscillatory-zoned rim	0.00581	0.00106	0.00082	0.00008	0.53712	0.05157	0.00797	0.83594	0	1	0	1	0	5.2	0.5	569	896	0.63	
KRG16-101-36	oscillatory-zoned rim	0.00613	0.00383	0.00081	0.00008	0.14815	0.05458	0.03377	0.83594	0	1	0	1	0	5.2	0.5	82	147	0.56	

n.d.: not determined

Table S2b. Results of LA－ICP－MS U－Pb zircon dating with common Pb correction assuming initial disequilibrium.

analysis no.	microtexture	$^{207}Pb/^{235}U$	error (1σ)	$^{206}Pb/^{238}U$	error (1σ)	Error correlation	$^{207}Pb/^{206}Pb$	error (1σ)	common $^{207}Pb/^{206}Pb$	error	$f_{Th/U}$	error (30%)	$f_{Pa/U}$	error (30%)	Disequilibrium & Common Pb corrected age (Ma)	error (1σ)	Th (ppm)	U (ppm)	Th/U	* excluded from weighted average
KRG16-101-1	unzoned mantle	8.40462	0.76642	0.07334	0.00608	0.90954	0.83109	0.03150	0.83594	0	0.122271	0.036681	3.36	1.008	456.4	36.6	n.d.	n.d.	n.d.	*
KRG16-101-2	oscillatory-zoned rim	0.00639	0.00106	0.00078	0.00005	0.41295	0.05964	0.00901	0.83594	0	0.122271	0.036681	3.36	1.008	5.0	0.3	629	739	0.85	
KRG16-101-3	oscillatory-zoned rim	0.00531	0.00085	0.00079	0.00007	0.53741	0.04874	0.00655	0.83594	0	0.122271	0.036681	3.36	1.008	5.2	0.4	600	893	0.67	
KRG16-101-4	oscillatory-zoned rim	0.00568	0.00096	0.00081	0.00006	0.44623	0.05104	0.00774	0.83594	0	0.122271	0.036681	3.36	1.008	5.3	0.4	391	674	0.58	
KRG16-101-5	unzoned mantle	0.00610	0.00153	0.00086	0.00006	0.29956	0.05130	0.01231	0.83594	0	0.122271	0.036681	3.36	1.008	5.6	0.4	269	379	0.71	
KRG16-101-6	oscillatory-zoned rim	0.02174	0.00997	0.00326	0.00146	0.97558	0.04835	0.00487	0.83594	0	0.122271	0.036681	3.36	1.008	21.0	6.5	n.d.	n.d.	n.d.	*
KRG16-101-7	unzoned mantle	0.00597	0.00089	0.00080	0.00006	0.48540	0.05444	0.00707	0.83594	0	0.122271	0.036681	3.36	1.008	5.2	0.3	1453	1132	1.28	
KRG16-101-8	unzoned mantle	25.41318	6.34566	0.21903	0.05350	0.97819	0.84149	0.04364	0.83594	0	0.122271	0.036681	3.36	1.008	1276.9	289.3	n.d.	n.d.	n.d.	*
KRG16-101-9	oscillatory-zoned rim	0.00515	0.00070	0.00078	0.00008	0.75091	0.04759	0.00427	0.83594	0	0.122271	0.036681	3.36	1.008	5.2	0.5	1064	1846	0.58	
KRG16-101-10	unzoned	9.41347	1.10182	0.08136	0.00890	0.93451	0.83913	0.03496	0.83594	0	0.122271	0.036681	3.36	1.008	504.3	53.3	n.d.	n.d.	n.d.	*
KRG16-101-11	oscillatory-zoned rim	0.00973	0.00353	0.00089	0.00010	0.32086	0.07917	0.02724	0.83594	0	0.122271	0.036681	3.36	1.008	5.6	0.6	404	949	0.43	
KRG16-101-12	oscillatory-zoned rim	0.00601	0.00177	0.00084	0.00008	0.32705	0.05166	0.01438	0.83594	0	0.122271	0.036681	3.36	1.008	5.5	0.5	169	327	0.52	
KRG16-101-13	oscillatory-zoned rim	0.00702	0.00222	0.00087	0.00011	0.38820	0.05825	0.01693	0.83594	0	0.122271	0.036681	3.36	1.008	5.7	0.6	221	343	0.64	
KRG16-101-14	oscillatory-zoned rim	0.00575	0.00129	0.00082	0.00006	0.34910	0.05082	0.01064	0.83594	0	0.122271	0.036681	3.36	1.008	5.4	0.4	317	541	0.59	
KRG16-101-15	oscillatory-zoned rim	0.00523	0.00230	0.00079	0.00007	0.20054	0.04816	0.02073	0.83594	0	0.122271	0.036681	3.36	1.008	5.2	0.4	203	221	0.92	
KRG16-101-16	oscillatory-zoned rim	0.00659	0.00165	0.00085	0.00007	0.31936	0.05597	0.01331	0.83594	0	0.122271	0.036681	3.36	1.008	5.5	0.4	296	426	0.69	
KRG16-101-17	oscillatory-zoned rim	0.00682	0.00164	0.00082	0.00007	0.35975	0.05997	0.01344	0.83594	0	0.122271	0.036681	3.36	1.008	5.3	0.4	321	420	0.76	
KRG16-101-18	oscillatory-zoned rim	0.00811	0.00257	0.00086	0.00008	0.28748	0.06846	0.02080	0.83594	0	0.122271	0.036681	3.36	1.008	5.5	0.5	204	256	0.80	
KRG16-101-19	oscillatory-zoned rim, crack	0.00849	0.00317	0.00083	0.00008	0.24292	0.07388	0.02676	0.83594	0	0.122271	0.036681	3.36	1.008	5.3	0.5	206	190	1.08	*
KRG16-101-20	oscillatory-zoned rim, crack	0.00654	0.00146	0.00083	0.00006	0.32817	0.05749	0.01211	0.83594	0	0.122271	0.036681	3.36	1.008	5.3	0.4	341	461	0.74	*
KRG16-101-21	oscillatory-zoned rim	0.00668	0.00259	0.00083	0.00007	0.21654	0.05806	0.02196	0.83594	0	0.122271	0.036681	3.36	1.008	5.4	0.4	116	224	0.52	
KRG16-101-22	oscillatory-zoned rim	0.00558	0.00066	0.00078	0.00004	0.45816	0.05208	0.00550	0.83594	0	0.122271	0.036681	3.36	1.008	5.1	0.3	879	1840	0.48	
KRG16-101-23	unzoned rim	0.01410	0.00574	0.00092	0.00007	0.17825	0.11140	0.04459	0.83594	0	0.122271	0.036681	3.36	1.008	5.5	0.5	124	254	0.49	
KRG16-101-24	oscillatory-zoned rim	0.00573	0.00151	0.00078	0.00007	0.33107	0.05362	0.01333	0.83594	0	0.122271	0.036681	3.36	1.008	5.1	0.4	275	477	0.58	
KRG16-101-25	unzoned	4.92068	0.77426	0.04267	0.00642	0.95639	0.83631	0.03844	0.83594	0	0.122271	0.036681	3.36	1.008	269.5	39.8	n.d.	n.d.	n.d.	*
KRG16-101-26	unzoned	8.65497	1.09942	0.07489	0.00879	0.92402	0.83815	0.04071	0.83594	0	0.122271	0.036681	3.36	1.008	465.7	52.9	n.d.	n.d.	n.d.	*
KRG16-101-27	unzoned	7.94481	1.06792	0.06892	0.00861	0.92955	0.83603	0.04143	0.83594	0	0.122271	0.036681	3.36	1.008	429.8	52.2	n.d.	n.d.	n.d.	*
KRG16-101-28	unzoned	8.76559	1.69260	0.07486	0.01396	0.96585	0.84928	0.04249	0.83594	0	0.122271	0.036681	3.36	1.008	465.4	84.3	n.d.	n.d.	n.d.	*
KRG16-101-29	oscillatory-zoned rim	0.00812	0.00132	0.00087	0.00010	0.73813	0.06786	0.00746	0.83594	0	0.122271	0.036681	3.36	1.008	5.5	0.6	596	1076	0.55	
KRG16-101-30	oscillatory-zoned rim	0.00669	0.00276	0.00092	0.00009	0.22815	0.05299	0.02129	0.83594	0	0.122271	0.036681	3.36	1.008	6.0	0.5	114	195	0.58	
KRG16-101-31	oscillatory-zoned rim	0.03772	0.01384	0.00105	0.00013	0.33810	0.26046	0.08995	0.83594	0	0.122271	0.036681	3.36	1.008	5.0	0.9	555	565	0.98	
KRG16-101-32	oscillatory-zoned rim	0.00620	0.00139	0.00081	0.00005	0.28156	0.05527	0.01186	0.83594	0	0.122271	0.036681	3.36	1.008	5.3	0.3	340	566	0.60	
KRG16-101-33	unzoned	6.85524	0.64235	0.05887	0.00498	0.90367	0.84459	0.03389	0.83594	0	0.122271	0.036681	3.36	1.008	368.8	30.4	n.d.	n.d.	n.d.	*
KRG16-101-34	unzoned, crack	9.95498	1.52518	0.08506	0.01234	0.94689	0.84878	0.04181	0.83594	0	0.122271	0.036681	3.36	1.008	526.4	73.7	n.d.	n.d.	n.d.	*
KRG16-101-35	oscillatory-zoned rim	0.00581	0.00106	0.00082	0.00008	0.53712	0.05157	0.00797	0.83594	0	0.122271	0.036681	3.36	1.008	5.3	0.5	569	896	0.63	
KRG16-101-36	oscillatory-zoned rim	0.00613	0.00383	0.00081	0.00008	0.14815	0.05458	0.03377	0.83594	0	0.122271	0.036681	3.36	1.008	5.3	0.5	82	147	0.56	

n.d. : not determined